Method for deriving telescope specifications for Earth-detecting coronagraphs and its use in prioritizing technology development investments

Bijan Nemati [a], H. Philip Stahl [b]

[a] University of Alabama in Huntsville, 301 Sparkman Dr., Huntsville, AL 35899, U.S.A.;
[b] Marshall Space Flight Center, Huntsville, AL 35811

Executive Summary

Different potential exoplanet mission concepts require different enabling and enhancing technologies. Decisions regarding prioritizing the development of these technologies can be made using a Science-Driven Systems-Engineering framework. The white paper makes the following specific recommendations. (1) Any potential telescope/coronagraph combination should develop a wavefront stability error budget using the method described in this white paper. That error budget will inform discussions about what technology development will be needed to enable the mission. (2) Enhancing and enabling technologies requiring investment include: low noise reaction wheels or control moment gyros; micro-thruster technology; active vibration isolation; materials and design practice for making lightweight stiff structures and optical components; 200-Hz wavefront sensing and control; 500-Hz sub-picometer-precision edge sensor and position actuators; non-destructive process to quantify CTE homogeneity of 4-m class mirrors to an uncertainty of +/- 1 ppb/K over a 100 x 100 sampling; laser gauge positional metrology system; and predictive active thermal control.

Introduction

Performing exoplanet science with an internal coronagraph requires an ultra-stable telescope wavefront to provide an ultra-stable point spread function (PSF) for the coronagraph to block. An unstable wavefront produces noise in the dark hole which impacts the ability to detect and characterize an exoplanet. For example, to image Earth from a distance of 10 parsecs requires a coronagraph that can suppress the Sun's light by a factor of 10^{10} to 10^{11} at an angular separation of 100 milli-arc-second (maximum elongation). At quadrature phase, our Earth, with a geometric albedo of 0.37, has a flux ratio relative to the sun of 2.1×10^{-10}, or 210 ppt (parts-per-trillion). Thus, to directly image Earth with a signal-to-noise ratio (SNR) of 7, requires that the noise-equivalent flux ratio (NEFR) of the processed final image (after coronagraph suppression) from the host star must not exceed 30 ppt. There are two sources for NEFR: photometric and systematic. Photometric noise includes photon and detector noise. Systematic noise are caused by disturbances such as wavefront stability.

This paper describes a systems engineering process for deriving a wavefront stability specification that can be applied to any potential telescope/coronagraph combination. To illustrate the process, error budgets for four representative architectures are derived:

- 4-meter off-axis unobscured circular monolithic primary mirror with 3 different coronagraphs:
  - Vector-Vortex Charge 4 Coronagraph
  - Vector-Vortex Charge 6 Coronagraph
  - Hybrid Lyot Coronagraph
- 6-meter on-axis hex-segmented aperture primary mirror (similar to Webb telescope) with an apodized pupil Lyot coronagraph (APLC) originally designed for ATLAST.

As this white paper shows, for these cases, mid-spatial frequency wavefront stability is critical to exoEarth science. And the tolerances for each error budget help to identify what technology investments are needed to enable exo-Earth science with that architecture.

Please note that the error budget derived in this white paper and its implications are for coronagraphy only. This white paper is not relevant to a star-shade nor non-coronagraphy general astrophysics missions. Finally, this white paper is based on work listed in the Bibliography.

Definitions

Before presenting the process by which the error budget is created, some terms need definition.

Core Throughput is defined as the fraction of the planet light entering the telescope that ends up inside the planet PSF's core region – which is defined as the area circumscribed by its half-max contour. Photometric SNR is influenced most strongly by the high-signal part of the PSF, and the core is a good representation of that domain. For an unobscured circular primary mirror, the core is a circle of diameter very nearly equal to 1 λ/D. Core throughput includes two effects: the geometric loss of light due to partial or complete obscuration by the coronagraph masks and/or telescope secondary mirror, and associated diffraction spreading.

Inner Working Angle (IWA) is defined as the angular separation from line of sight (to the science star) below which the azimuthally averaged core throughput falls below 1/2 of its maximum value within the dark hole. For example, Figure 1 shows the azimuthally averaged throughput for four telescope/coronagraph combinations (off-axis 4-m circular unobscured telescope with three different coronagraphs, and on-axis 6.5-m segmented aperture telescope with an apodized pupil Lyot coronagraph). For the VVC-4, its maximum throughput is 38% and its IWA is 1.6 λ/D (~40 mas). However, please note that its inner working angle is not the closest separation at which effective imaging can take place. In this example, the VVC-4 coronagraph shows good throughput (>5%), all the way down to1.0 λ/D (~25 mas).

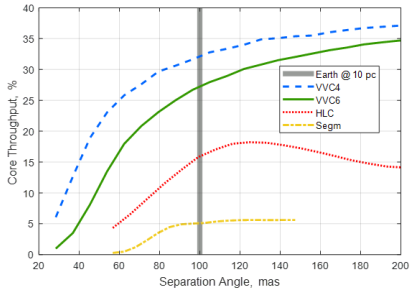

Figure 1: Throughput vs angle for 4 cases. 100 mas is separation for Exo-Earth at 10 pc.

The smaller the IWA and the larger the throughput, the greater the number of habitable zones that can be searched. The ability to achieve a small IWA depends upon the telescope's ability to produce a small stable point spread function (PSF) with a compact stable encircled energy (EE). The smaller the EE, the smaller the IWA. It is common knowledge that the larger a telescope's aperture, the smaller its PSF and EE. But, what is often overlooked is that an unobscured (off-axis) telescope always has a more compact EE (better IWA) than an on-axis telescope with a central obscuration – because diffraction from the central obscuration broadens the PSF. To be specific, an unobscured circular aperture has 82.8% EE at λ/D. And, a telescope with a 10% central obscuration has 82.5% EE at 1.4 λ/D (and for a 20% obscuration, 82% EE is at 1.63 λ/D). Thus to achieve the same IWA performance as an unobscured 4-m telescope, an on-axis telescope with 10% central obscuration would need to be at least 5.6-m and one with 20% obscuration would need to be at least 6.5-m. Additionally, diffraction from secondary mirror spider obscurations distort the PSF and broaden the EE. A 1 to 2% wide spider can increase EE diameter (IWA) by 5 to 10% – requiring a 5 to 10% larger on-axis telescope. Of course the problem is even worse for a segmented aperture primary mirror.

Raw Contrast is the measure of the coronagraph's effectiveness in suppressing starlight near the planet. It is defined as the ratio of the line-of-sight throughput of the science star's light divided by its throughput if the star was at the planet's location. In this definition, the denominator at first seems counter-intuitive, since the star is never placed at the planet's location. But, defining contrast in this way makes the correspondence between flux ratio (a planet attribute) and contrast (an instrument attribute) more explicit. The "raw" qualifier distinguishes it from residual contrast after differential imaging and other post-processing.

Deriving a Performance Specification

The first step in creating a wavefront stability error budget is to allocate the desired science sensitivity (i.e. 30 ppt for an exo-Earth at 10 pc) between photometric and systematic noise. This is done via an integration time analysis.

Integration Time is key for many reasons. It is needed to reduce the effect of random noise. But, other errors (such as thermal errors or actuator drift) actually grow with time. Success in direct detection of a planet can be parameterized in terms of the achieved SNR in a given amount of time, or conversely the time required to achieve a desired SNR. This time defines the maximum desired duration for the telescope's wavefront stability.

For example, assuming an Earth-like planet around a sun-like star at 10 pc distance with a 3-solar exo-zodi brightness, Figure 2 shows the contributions of the main categories of error to the flux ratio noise for a VVC-6 coronagraph. Figure 2(a) shows the SNR after a total integration time of 25 hours, as well as the time to reach SNR = 7. These are plotted against residual speckle noise. If this noise is 23-ppt, SNR of 7 is achieved in 25 hrs. If it is 16-ppt, SNR of 7 is achieved in 16 hrs. Figure 2(b) shows the relative contributions to the flux ratio noise from the main noise sources for a range of integration times from 5 to 25 hrs. The horizontal line signifies total allowable error for seeing an exo-Earth with an SNR of 7, namely a total NEFR of 30 ppt. The random contributions are calculated versus integration time, and rolled up into a total random error. The quadrature difference of the total allowable error on the random roll-up is the allowable residual speckle error. At 25 hrs of integration time, the random errors add in quadrature to a total of about 16 ppt, leaving a little over 25 ppt that can be assigned to residual speckle noise and reserve. To allocate more noise to systematic error sources, the contribution from random errors can be further reduced by integrating longer. But this will require the telescope to be stable for the longer integration period.

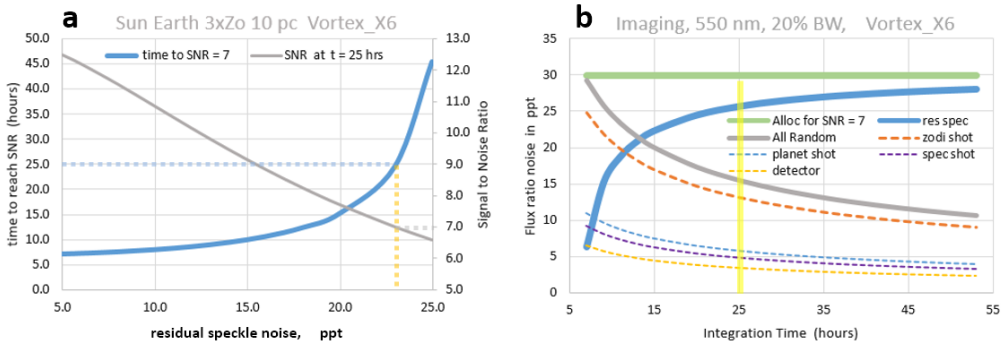

Figure 2: Contributions of different categories of noise to the estimation of the planet flux ratio for an Earth-like planet orbiting at 1AU around a Sun-like star which is 10 pc away with exo-zodi level that is 3 times denser than solar. The orbital phase angle is assumed to be 90 degrees. The horizontal axis is the standard deviation of the residual speckle after differential imaging and post processing, in parts per trillion (ppt). The left plot (labeled "a") shows the time to reach SNR and the achievable SNR, as the residual speckle is increased, while the right plot (labeled "b") shows the relative contributions to the flux ratio noise from the main noise sources assuming an integration time of 50 hrs.

The second step in creating a wavefront stability error budget is to insert the random and systematic error allocations into a top-level error budget (Figure 3) and flow the systematic error down to a telescope stability allocation. Most coronagraphs employ some form of differential imaging to account for the speckle pattern that is otherwise a confusion background in the final image. Reference Differential Imaging (RDI), which is baselined for the WFIRST coronagraph, is a common choice. RDI turns the contrast (C) requirement into a more tractable contrast *stability* (ΔC) requirement. Additionally, further suppression can be achieved by various post processing methods that keep track of instrument operational parameters. Assuming that a mission uses RDI with post processing and that this post processing provides a suppression of $f_{pp} = 0.5$, we have a telescope contrast stability allocation of 40 ppt.

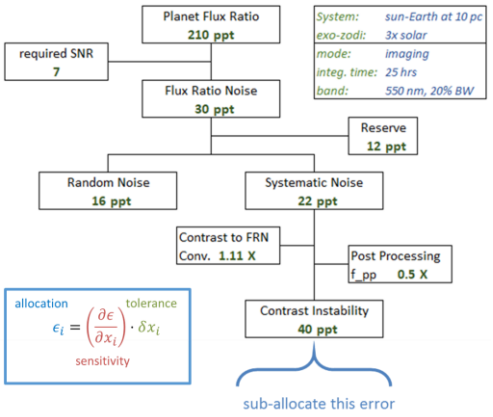

Figure 3: Wavefront Stability Error Budget flow-down

The third step is to flow the 40 ppt ΔC allocation down into individual error components, by calculating the contrast sensitivity to each term. Contrast Sensitivity is how much residual raw contrast is introduced into the dark-hole as a function of wavefront error. It is determined by sequentially adding, for each wavefront error mode, some amount of wavefront perturbation (say 10 picometers amplitude) into a coronagraph model and calculating the change in the contrast 'leakage'. This wavefront error can be described by spatial frequencies or Zernike polynomials or even Seidel aberrations. Because of the coherent mixing of the perturbation field with the existing field, this all has to be done with a stipulated initial contrast. The initial contrast assumed becomes the requirement on the coherent part of the raw contrast for the instrument.

Figure 4 shows a representative output for the (Monolith/VVC6) case exposed to a wavefront error perturbation of 10 pm PV trefoil. The residual speckle map (labeled ΔC) is shown on the left. This map is then divided in annular rings. For each annular region, the standard deviation $\sigma_{\Delta C}$ is computed giving the respective azimuthally averaged residual speckle. The right hand contour plot shows how the residual speckle spatial noise varies with radial slice and with perturbation amplitude. If we set a requirement, from error budgeting, that the contribution from this perturbation (i.e. trefoil) cannot exceed 1e-11, then the region excluded is that shaded in light red in the figure. This implies that for the level of initial contrast we started with, and for a requirement of $\sigma_{\Delta C}$ < 1e-11, the trefoil change between reference and target star observation times must be kept under about 12 pm PV.

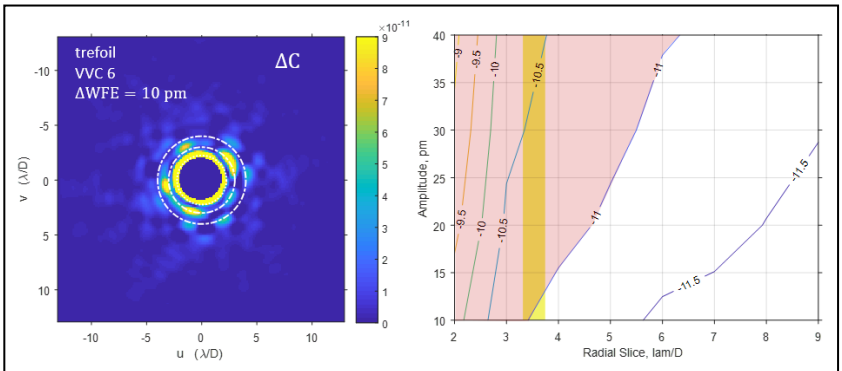

Figure 4: Residual speckle (left) and contours of $\sigma_{\Delta C}$ for different levels of perturbation wavefront error amplitude and radial slice. These plots correspond to the case of trefoil mode on vector vortex charge 6 coronagraph. The vertical yellow strip is centered at the separation of the reference case (exo-Earth at 10 pc) observed at a waveband centered at 550 nm. On the left image a 1 λ/D wide annular region at this separation is highlighted by a pair of concentric circles.

Repeating this process for all of the wavefront error modes generates a summary graph for each aberration. Figure 5 shows the results for each case studied. The vertical line at 10^{-10} raw contrast indicates the target goal needed to observe an exo-Earth. The horizontal line at 10^{-11} delta-contrast indicates a possible error budget allocation for 10 pm PV of each error. As long as the lines are below the horizontal line, the coronagraph should be able to detect an exo-Earth.

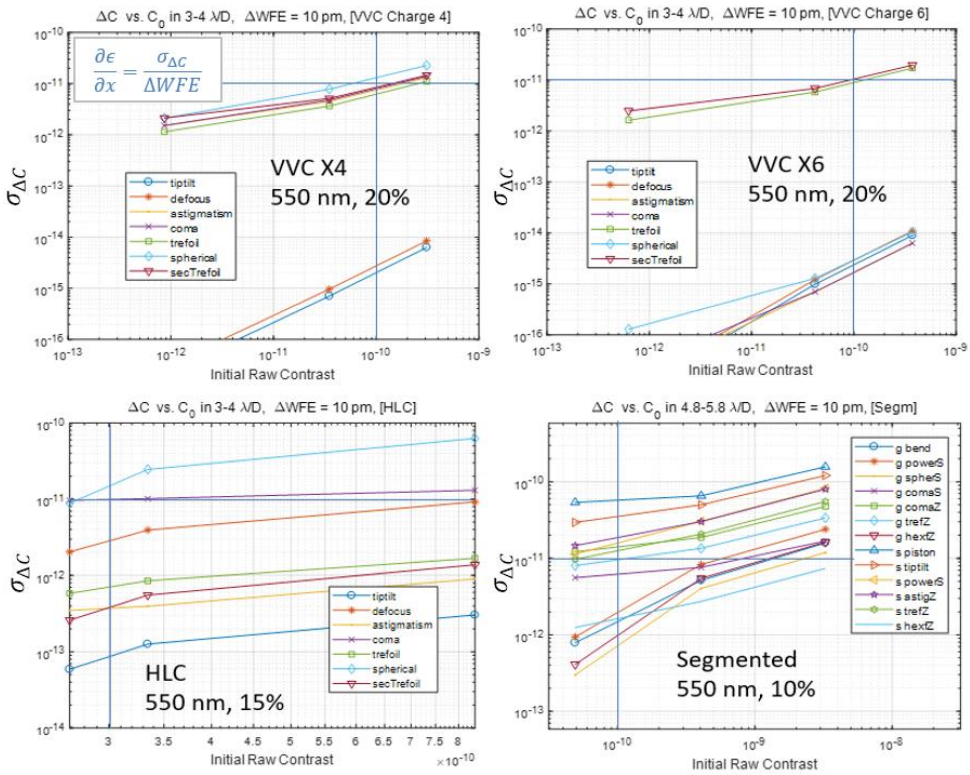

Figure 5: Dependence of $\sigma_{\Delta C}$ on initial raw contrast for a perturbation with a peak to valley amplitude of 10 pm in each of the given modes for each of the four cases studied. $\sigma_{\Delta C}$ is computed for a 1 λ/D slice centered on the working angle of the reference case planet (exo-Earth at 10 pc). In the segmented case, the diameter of the primary is larger, reducing λ/D, and increasing the working angle at which the exo-Earth appears. All four cases were evaluated for a center wavelength of 550 nm, with the maximum bandwidth allowable by the design.

In the two vector vortex cases there are clearly two populations: those to which the coronagraph is very insensitive and those with higher sensitivity. The difference in sensitivity is over 3 orders of magnitude. In the charge 6 case, only trefoil and secondary trefoil are important. In the charge 4 case, spherical and coma also matter.

Please note that the HLC and segmented APLC (ATLAST) designs are relatively older and do not necessarily represent the best performance possible by these approaches. The HLC case cannot reach the nominal 1e-10 raw contrast, but its sensitivities to the various modes is mostly good. In the segmented case, the larger diameter means that the same planet can be seen at a larger working angle (5.3 λ/D).

The fourth step is to convert the delta-contrast error budget allocations for each wavefront error into physical tolerances. These are the performance specifications that the telescope in each case study must achieve to detect an exo-Earth. Figure 6 shows the results for the monolithic mirror cases and Figure 7 shows the segmented mirror with ALPC results. The errors shown in Figures 6 and 7 were selected based on their likelihood of occurring.

Figure 6 contains two classes of errors, global and mirror errors. Global errors are produced by rigid body motion of the primary relative to the secondary mirror. For example, defocus and spherical are produced by the PM and SM moving towards or away from each other (Z-axis). For an on-axis telescope, coma is produced by a lateral displacement between the PM and SM. But for an off-axis configuration, lateral displacement produces astigmatism and some coma. Errors such as astigmatism, trefoil and secondary trefoil are produced by the mirror bending on its mount under the influence of an acceleration force. The bottom 'tolerance' row for each coronagraph gives the telescope's wavefront stability tolerance for each error. It is calculated by dividing a contrast allocation for that error by the coronagraph's sensitivity to that error. As expected, the VVC-6 tolerances for tip/tilt, defocus, astigmatism, coma and spherical are very large (i.e. 5 to 10 nm PV) because the VVC-6 is insensitive to these errors. By contrast, the tolerance for trefoil and secondary trefoil is small (30 picometers). At 30 picometers, trefoil and secondary trefoil each contribute about 30 ppt of contrast instability. Please note that the allocations are based on a 100 ppt NEFR. To get to a 40 ppt NEFR, multiple the results by 0.4. All of the other errors combined contribute less than 10 ppt. Similarly, for the VVC-4, only tip/tilt and defocus have large tolerances. And, for the hybrid-Lyot, the tolerance for all aberrations are small. Finally, all Figure 6 specifications are peak-to-valley.

VVC 6

(C0 = 100 ppt)	tiptilt	defocus	astigmatism	coma	trefoil	spherical	secTrefoil
Sensitivities (ppt/pm)	0.00024	0.00029	0.00017	0.00017	0.90	0.00029	1.04
Allocations (ppt)	1.52	1.52	1.52	1.52	27.5	1.52	28.9
Tolerances (pm)	6361	5170	9095	9026	30	5196	28

VVC 4

(C0 = 100 ppt)	tiptilt	defocus	astigmatism	coma	trefoil	spherical	secTrefoil
Sensitivities (ppt/pm)	0.00020	0.00027	0.77	0.82	0.64	1.35	0.86
Allocations (ppt)	1.10	1.10	16.9	18.0	14.0	20.8	18.8
Tolerances (pm)	5427	3996	22	22	22	15	22

HLC

(C0 = 300 ppt)	tiptilt	defocus	astigmatism	coma	trefoil	spherical	secTrefoil
Sensitivities (ppt/pm)	0.0095	0.305	0.037	0.990	0.073	1.738	0.042
Allocations (ppt)	1.4	8.8	1.4	27.5	2.1	27.5	1.4
Tolerances (pm)	153	29	39	28	29	16	35

Figure 6: Performance Tolerances in units of picometers peak-to-valley for an off-axis unobscured circular aperture telescope as a function of coronagraph type.

Figure 7 also contains two classes of aberrations, global and segment level errors. Global errors for the segmented telescope are the same as for the monolithic, except for global bend. Global bend is bending of the structure to which the segments are mounted. In this case, the piston and tip tilt of a tangent plane for each segment is also calculated. To estimate the effect of segment level errors (piston, tip/tilt, defocus, astigmatism, trefoil), a number of instances are randomly create with different azimuthal orientation (clocking) then averaged. As with Figure 6, the allocations are based on a 100 ppt NEFR. To get to a 40 ppt NEFR, simply multiple the results by 0.4. Finally, in Figure 7, the global specification results are PV but the segment level specifications are RMS.

Segm

(C0 = 100 ppt)	g_bend	g_powerS	g_spherS	g_comaS	g_comaZ	g_trefZ	g_hexfZ	s_piston	s_tiptilt	s_powerS	s_astigZ	s_trefZ	s_hexfZ
Sensitivities (ppt/pm)	0.15	0.21	0.090	0.59	1.32	0.89	0.12	5.53	3.26	1.44	1.71	1.14	0.15
Allocations (ppt)	2.3	3.3	1.4	9.1	14.7	13.8	1.9	14.7	14.7	14.7	14.7	14.7	2.3
Tolerances (pm)	15.5	15.5	15.5	15.5	11.2	15.5	15.5	2.7	4.5	10.2	8.6	12.9	15.5

peak to valley | standard deviation

Figure 7: Performance Tolerances in units of picometers peak-to-valley and RMS for an on-axis centrally-obscured segmented aperture telescope with an Apodized Pupil Lyot Coronagraph (APLC).

The final step is to distribute contrast allocation according to likelihood of each error occurring. Figure 8 provides a Zernike polynomial based error budget for a 4-m off-axis telescope with a VVC-6. The right hand column titled 'WFE Tolerance' is the maximum allowed telescope WFE for each Zernike term based on a distribution of 40 ppt of contrast. The distribution of contrast is determined by the sensitivity of the coronagraph to each aberration term and the likelihood, from STOP (structural thermal optical performance) modeling, that each aberration term will occur. STOP modeling provides predictions for how much aberration will be caused by LOS jitter (from mechanical vibration), the PM bouncing on its mirror in response to mechanical accelerations (Inertial error), and thermal drift cause by pointing the telescope relative to the sun.

Baseline HabEx 4-m Error Budget for VVC-6 for 2.4 to 3.4 l/D

Order				Predicted Performance Amplitude [pm rms]			Total WFE	VVC-6 Sensitivity	Raw Contrast	Allocation	WFE Tolerance	
K	N	M	Aberration	LOS	Inertial	Thermal	[pm PV]	[ppt/pm PV]	[ppt]	[ppt]	[pm RMS]	Aberration
			TOTAL RMS	3.607	1.976	4.424	13.391		10.936	40.000	22.094	TOTAL RMS
1	1	1	Tilt	1.103	0.103	1.902	4.403	0.0002	0.001	0.003	8.051	Tilt
2	2	0	Power (Defocus)	2.945	1.079	1.844	6.301	0.0003	0.002	0.008	13.306	Power (Defocus)
3	2	2	Pri Astigmatism	1.723	1.327	2.957	8.992	0.0002	0.002	0.006	13.427	Pri Astigmatism
4	3	1	Pri Coma	0.388	0.041	0.522	1.844	0.0002	0.000	0.001	2.385	Pri Coma
5	3	3	Pri Trefoil	0.019	0.950	1.826	5.822	1.0016	5.831	21.329	7.529	Pri Trefoil
6	4	0	Pri Spherical	0.009	0.182	0.346	0.874	0.0003	0.000	0.001	1.430	Pri Spherical
7	4	2	Sec Astigmatism	0.007	0.064	0.124	0.441	1.6495	0.728	2.662	0.510	Sec Astigmatism
8	4	4	Pri Tetrafoil	0.000	0.087	0.123	0.478	0.9312	0.445	1.626	0.552	Pri Tetrafoil
9	5	1	Sec Coma	0.001	0.002	0.083	0.289	1.6645	0.481	1.759	0.305	Sec Coma
10	5	3	Sec Trefoil	0.000	0.129	0.171	0.742	1.8200	1.351	4.942	0.784	Sec Trefoil
11	5	5	Pri Pentafoil	0.000	0.057	0.132	0.498	2.4409	1.216	4.447	0.526	Pri Pentafoil
12	6	0	Sec Spherical	0.000	0.015	0.005	0.041	2.8902	0.119	0.433	0.057	Sec Spherical
13	6	2	Ter Astigmatism	0.000	0.007	0.010	0.046	2.7219	0.125	0.456	0.045	Ter Astigmatism
14	6	4	Sec Tetrafoil	0.000	0.008	0.004	0.034	2.2050	0.075	0.273	0.033	Sec Tetrafoil
15	6	6	Pri Hexafoil	0.000	0.000	0.013	0.049	3.1667	0.154	0.563	0.048	Pri Hexafoil
16	7	1	Ter Coma	0.000	0.000	0.007	0.028	3.0608	0.084	0.308	0.025	Ter Coma
17	7	3	Ter Trefoil	0.000	0.009	0.021	0.092	2.7946	0.258	0.943	0.084	Ter Trefoil
18	7	5	Sec Pentafoil	0.000	0.000	0.005	0.021	3.0694	0.064	0.233	0.019	Sec Pentafoil
19	7	7	Pri Septafoil	0.000	0.000	0.000	0.000	2.6510	0.001	0.005	0.000	Pri Septafoil

Figure 8: Error budget for 4-m off-axis monolithic aperture telescope and vector vortex charge 6 coronagraph.

Finally, many may be familiar with a wavefront stability vs VVC charge # table published by Ruane in 2017 (Figure 9). The values in this table are the maximum error per Zernike if all of the NEFR was allocated to that mode.

Aberration	Indices		Allowable RMS wavefront error (nm) per mode			
	n	*m*	charge 4	charge 6	charge 8	charge 10
Tip-tilt	1	±1	1.1	5.9	14	26
Defocus	2	0	0.8	4.6	12	26
Astigmatism	2	±2	0.0067	1.1	0.90	5
Coma	3	±1	0.0062	0.66	0.82	5
Spherical	4	0	0.0048	0.51	0.73	6
Trefoil	3	±3	0.0072	0.0063	0.57	0.67
2nd Astig.	4	±2	0.0080	0.0068	0.67	0.73
2nd Coma	5	±1	0.0036	0.0048	0.69	0.85
2nd Spher.	6	0	0.0025	0.0027	0.84	1
Quadrafoil	4	±4	0.0078	0.0080	0.0061	0.53
2nd Trefoil	5	±3	0.0051	0.0056	0.0043	0.72
3rd Astig.	6	±2	0.0023	0.0035	0.0034	0.81
3rd Coma	7	±1	0.0018	0.0022	0.0036	1.18
3rd Spher.	8	0	0.0018	0.0018	0.0033	1.49

Garreth Ruane, June 2017

not rejected
first-order rejection
> first-order rejection

Figure 9: Wavefront Stability Required by VVC

Error Budget Implications

The most important conclusion to be drawn from Figure 6 to 8 is that exoEarth science requires a telescope with picometer mid-spatial frequency wavefront stability. For a segmented aperture telescope, the most important error sources are segment level rigid body motions of piston and tip/tilt (Figure 7). For a monolithic aperture telescope with a VVC-6 the most important errors (i.e. the modes getting the largest NEFR allocations) are trefoil, secondary trefoil and primary pentafoil (Figure 8). For a monolithic telescope with a VVC-4, astigmatism is also an important error. The primary source of these errors are from interaction between the primary mirror and its mount in response to mechanical vibration and thermal drift. For higher order terms, STOP analysis indicates that the largest potential error source is coefficient of thermal expansion (CTE) inhomogeneity in the primary mirror. CTE homogeneity is also important for a segmented aperture telescope, as CTE inhomogeneity can produce errors in the segments that will impact the dark-hole.

The second most important conclusion to draw from the error budget analysis is that different telescope/coronagraph combinations require different technologies to enable their mission concept architecture. A segmented mirror architecture needs a technology to minimize segment level piston and tip/tilt error, and also back-plane bending. And both architectures require a technology for minimizing thermal deformations.

Technology Development Implications

Wavefront instability errors arise from two sources: mechanical and thermal. Mechanical disturbances excite inertial motion and vibrational modes in optical components and structure. These motions can cause line-of-sight errors (LOS jitter), segment level piston and tip/tilt, and bending of optical components as they react against their mounts. Thermal errors occur when a telescope is slewed relative to the Sun. Its thermal load changes cause the structure holding the mirrors to expand/contract (resulting in LOS error) and the mirrors themselves to change shape.

While not designed to meet the requirements of a UVOIR exoplanet science mission, JWST is an example of the current state of art. Figure 10 shows JWST's predicted response to its expected mechanical environment and Figure 11 shows JWST's predicted response to a worst case thermal slew. The JWST secondary mirror support structure has a first mode of ~7.5-Hz at its operating temperature of 50K. And, when excited by the reaction wheels, secondary mirror motion can impact JWST's LOS and WFE specifications. However, because of dampening, a warm JWST may have LOS stability consistent with the HabEx specification of <0.5-mas per axis. [Feinberg, et. al., "A Cost-effective and Serviceable ATLAST 9.2m Telescope Architecture", Proc. SPIE. 9143. (August 02, 2014) doi: 10.1117/12.2054915.] Similarly, the JWST primary mirror backplane structure has a 17-Hz bending mode and the individual segments have rocking modes (tip/tilt) in the 40-Hz range. When JWST slews from its coldest to its warmest pointing, its temperature is predicted to change by 0.22K and its WFE is predicted to change by 31 nm rms. While not designed to do exoplanet science, it would take JWST over 14 days to achieve the required thermal wavefront stability.

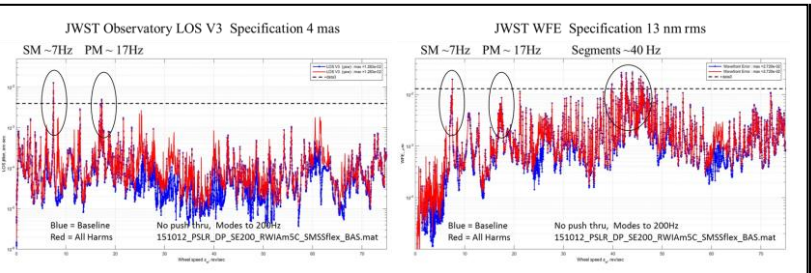

Figure 10: JWST cryogenic Line of Sight and Wavefront Error Performance Predictions [Mosier, Gary, Isolation Requirement, AMTD Report, 2014]

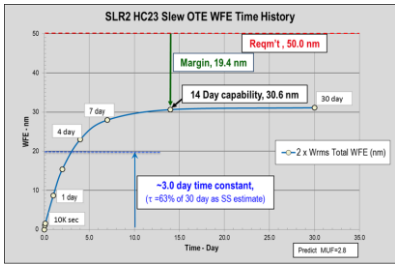

Figure 11: JWST thermal slew [13-JWST-0207 F, 2013]

Technology solutions to mitigate wavefront instability fall into four categories:

- Minimize the disturbance
- Minimize the transmission of the disturbance into to telescope.
- Minimize the response of the telescope to the disturbance
- Actively control the telescope's response to the disturbance

Minimizing Mechanical Disturbances: the best way to minimize mechanical disturbances, is to eliminate their source. Sources of mechanical disturbances include reaction wheels, control moment gyros, thruster, cryo-coolers or other mechanism. For example, invest in lower noise reaction wheels or control moment gyros. Or, invest in micro-thruster technology.

Minimizing Transmission of Mechanical Disturbances: the traditional method for minimizing the transmission of mechanical disturbances into a telescope is passive isolation. JWST uses two passive isolation stages. Another approach worthy of investment is active vibration isolation.

Minimizing Response of the Telescope: the best way to minimize the response of a structure to mechanical disturbance is to make it stiff. As illustrated in Figure 12 [Lake, Peterson, and Levine, *Rationale for defining Structural Requirements for Large Space Telescopes,* AIAA Journal of Spacecraft and Rockets, Vol. 39, No. 5, 2002.], wavefront error is proportional to rms magnitude of the applied inertial acceleration divided by square of the structure's first mode frequency. Thus, to achieve <10 pm rms errors requires either a very stiff system or very low acceleration loads. For a given stiffness mirror, a 10X reduction in acceleration results in a 10X WFE reduction. But for a given acceleration level, a 10X increase in stiffness results in a 100X WFE reduction. Therefore, technology investment in materials and design practice for making stiffer structures would be beneficial.

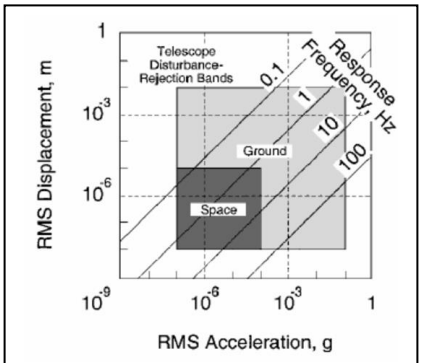

Figure 12: Error vs Load

Actively Controlling Response of the Telescope: the final solution for mitigating wavefront instability from mechanical sources is active control. Because, as illustrated in Figure 10, the response of telescopes to mechanical disturbances is in the 10 to 50-Hz range, wavefront sensing and control the control technology at a 200 Hz bandwidth is required to compensate for structural flexing. And 500-Hz sub-picometer-precision edge sensors and actuators are required to control segment level rigid body motion – piston and tip/tilt.

Minimizing Thermal Disturbances: while it is not possible (nor desirable) to turn off the sun, thermal disturbances can be minimized by carefully selecting a RDI reference star relative to the science observation star. To maintain a constant thermal load on the observatory, change between the reference and science stars by rotating the telescope around the sun vector.

Minimizing Transmission of Thermal Disturbances: the traditional method for minimizing the transmission of thermal disturbance into the telescope is passive thermal isolation via insulation. This is a fully mature technology and requires no additional development.

Minimizing Response of the Telescope: to minimize the response of any structure to a thermal disturbance, make the structure and its constituent components athermal. The 'ideal' way to do this is to make everything out of a material with a coefficient of thermal expansion (CTE) that is zero. But since such a material does not exist, the best approach is the make the entire structure and its components out of a material with a completely uniform CTE – such that when its temperature changes, everything changes together. Again, this is typically not possible. In practice, structures are designed to be athermal by combining materials with positive and negative CTEs. Recently the NASA SBIR program has invested in developing a method to insert negative CTE nanoparticles into structural materials to 'tune' their CTE. Similarly, the CTE of ULE® and Zerodur® can be 'tuned' to provide 'zero' CTE at specific temperatures.

For general astrophysics missions, athermal structural design and 'zero' CTE mirrors are TRL-9 and do not require investment. But, coronagraphy's need for stability imposes a new requirement on knowledge of the mirror's CTE homogeneity. Spatial variation in the primary and secondary mirror's CTE, i.e. its homogeneity, will produce wavefront error as a function of temperature. Currently, both Schott Zerodur® and Corning ULE® assert that they can make mirror substrates

with CTE homogeneity better than +/- 5 ppb/K. To keep the wavefront error from such a mirror to less than 10-pm PV, the mirror's temperature must be kept stable to less than 1-mK. Or, if the homogeneity is +/- 2.5 ppb/K, then the mirror only needs to be stable to 2-mK. Also, as shown in Figure 8, knowledge of spatial distribution of the error is important. And, unlike mechanical wavefront error which is mostly low-spatial-frequency, thermal WFE can have significant high-spatial-frequency content. To minimize cost and risk, it is important to quantify CTE homogeneity in a mirror blank as early in the fabrication process as possible.

Schott has the ability to measure CTE homogeneity with an uncertainty of +/- 1 ppb/K using the push rod dilatometer technique. BUT, this process is destructive. It requires rods of glass to be 'cut' from the blank. At present Schott only cuts these CTE rods from the perimeter of its mirror substrates. Thus, Schott is unable to provide CTE homogeneity over a 2D sampling of the actual mirror substrate. This is a potential performance risk. Therefore, investment is required to develop a non-destructive process to characterize CTE of a primary mirror substrate over a 2D spatial sampling of at least 100 x 100 with an uncertainty of +/- 1 ppb/K at each sample location and validate this process by measuring the mirror substrate's CTE at a statistical relevant sampling of locations via the accepted push rod dilatometer technique.

Actively Controlling Response of the Telescope: the final solution for mitigating wavefront instability from thermal sources is active control. Fortunately, thermal effects are slow and there are multiple potential active control systems. The engineering challenge is to keep the drift between corrections small. One solution is wavefront sensing and control. Another solution is laser metrology to sense, track and correct rigid body motion between optical components. A third solution is active thermal control.

Active control operates by insulating the telescope such that it is cold biased and then heating it to the operating temperature. Hubble operates this way. The current TRL-9 active thermal control is defined by the Harris Corp Spaceview^{TM} telescope's thermal control systems sensors which have a noise of ~50-mK and control their 1.1-m telescope to a temperature of 100-mK. [Harris Corporation, "SpaceviewTM 110 Satellite Imaging Solution" Specification Data Sheet, harris.com, 2019.] Predictive thermal control (PTC) - currently funded via an Astrophysics Division Directed Work Package – is a next generation active thermal control system (Figure 13) that uses physics-based modeling to actively control a zonal thermal environment so that, as the telescope slews, the mirrors never see a temperature change of more than 10-mK. Please note: it is not necessary to 'control' the mirror to 1-mK to keep it stable to 1-mK. The needed control is proportional to the mirror's mass and thermal capacity. The higher its mass and capacity, the easier it is to keep thermally stable. STOP analysis indicates that a 4-m monolithic mirror can be controlled to a stability of 1-mK with a system having 50-mk noise and 30 second control period.

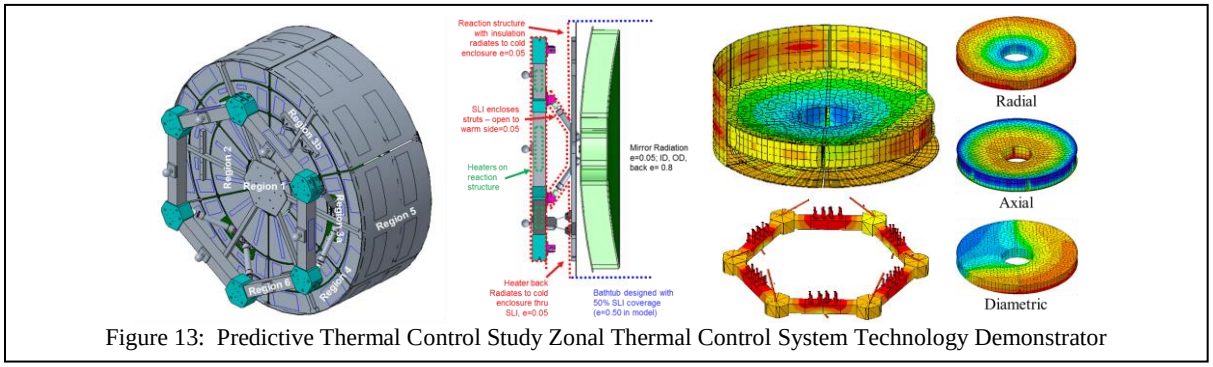

Figure 13: Predictive Thermal Control Study Zonal Thermal Control System Technology Demonstrator

Bibliography

1. Nemati, Bijan, H. Philip Stahl, Mark T. Stahl, Garreth Ruane, "HabEx Telescope WFE stability specification derived from coronagraph starlight leakage," Proc. SPIE 10743, Optical Modeling and Performance Predictions X, 107430G (17 September 2018)
2. Nemati, Bijan, Mark T. Stahl, H. Philip Stahl, Stuart B. Shaklan, "Effects of space telescope primary mirror segment errors on coronagraph instrument performance", Proc. SPIE 10398, UV/Optical/IR Space Telescopes and Instruments: Innovative Technologies and Concepts VIII, 103980G (5 September 2017); doi: 10.1117/12.2273072; http://dx.doi.org/10.1117/12.2273072
3. Stahl, H. Philip, "Advanced mirror technology development (AMTD) project: overview and year four accomplishments," Proc. SPIE 9912, Advances in Optical and Mechanical Technology for Telescopes and Instrumentation II, (22 July 2016); doi:10.1117/12.2234082
4. Stahl, Mark T., H. Philip Stahl, and Stuart B. Shaklan "Preliminary analysis of effect of random segment errors on coronagraph performance", Proc. SPIE. 9605, Techniques and Instrumentation for Detection of Exoplanets VII, 96050P. (September 24, 2015) doi: 10.1117/12.2190160
5. Stahl, H. Philip, "Overview and performance prediction of the baseline 4-meter telescope concept design for the habitable-zone exoplanet observatory", Proc. SPIE 10698, Space Telescopes and Instrumentation 2018: Optical, Infrared, and Millimeter Wave, 106980W (6 July 2018); doi: 10.1117/12.2315291; https://doi.org/10.1117/12.2315291
6. Harris Corporation, "PTC Thermal System Design Review", NASA Marshall Space Flight Center Contract NNM15AA01C, AMTD II, 17 July 2018,
7. Brooks, Thomas E., "Predictive thermal control applied to HabEx", Proc. SPIE 10398, UV/Optical/IR Space Telescopes and Instruments: Innovative Technologies and Concepts VIII, 1039814 (5 September 2017); doi: 10.1117/12.2274338